Electronic Supplementary Material (ESI) for Inorganic Chemistry Frontiers.

Supporting Information

Hollow Multi-shelled Structures SnO_2 with Enhanced Performance for Ultraviolet Photodetector

Meng Li, †[ab] Dan Mao, †[a] Jiawei Wan, †[a] Fakun Wang,[c] Tianyou Zhai,[c] Dan Wang*[ab]

[a] State Key Laboratory of Biochemical Engineering, Institute of Process Engineering, Chinese Academy of Sciences, 1North 2nd Street, Zhongguancun, Haidian District, Beijing 100190, P. R. China. E-mail: danwang@ipe.ac.cn

[b] School of Chemical Engineering, University of Chinese Academy of Sciences, No.19A Yuquan Road, Beijing, 100049, P. R. China.

[c] State Key Laboratory of Material Processing and Die & Mould Technology, School of Materials Science and Engineering, Huazhong University of Science and Technology, Wuhan, 430074, P. R. China.

Experimental Procedures

Synthesis of SnO_2 hollow multi-shelled structures: As reported in our previous work, Tin (IV) chloride pentahydrate ($SnCl_4 \cdot 5H_2O$) was used as the metal precursor. Carbonaceous microspheres (CMSs) were synthesized through the emulsion polymerization reaction of sucrose under the hydrothermal conditions as described elsewhere. Alkali-treated carbonaceous microspheres (ATCMSs) were prepared by immersing CMSs in a 0.05 M NaOH solution for 5 h. 1.0 g of ATCMSs was dispersed in 40 ml of 2 M tin(IV) chloride solution with the aid of ultrasonication for 20 min. After ultrasonic dispersion, the resulting suspension was aged for 5 h at room temperature, then filtered, washed with water and dried at 70^oC for 24 h. The resultant Sn^{4+} infused microspheres were heated to 50^oC in air at the rate of 1^oC min^{-1}, and kept at 500^oC for 2 h. The quadruple-shelled SnO_2 hollow microspheres were collected as white powers. Single-shelled, double-shelled, and triple-shelled SnO_2 hollow microspheres were synthesized by changing the concentration of chloride solution (0.1 M, 0.5 M, and 1 M, respectively) and using the same thermal procedure described above.

Device Fabrication: The SnO_2 HoMSs layer was deposited on Si/SiO_2 substrate by the screen-printing technique and the fabrication details are as follows: firstly, 50 mg of SnO_2 HoMSs powder was fully dispersed in C_2H_5OH solution with ultrasonication for 5 min. After then, 0.15g ethyl-cellulose, 0.3g alpha-terpineol and 20 μL acetic acid were added into the above mixture solution. The mixture is fully ground to produce the colloidal slurry. Then the slurry was deposited on Si/SiO_2 substrate by the screen-printing technique. Then the film was annealed at 450°C for 2 h in air with a heating rate of 2ºC/min to fabricate SnO_2 HoMSs film. Then, Cr/Au (200nm/800nm) electrodes were deposited on the SnO_2 HoMSs film by using magnetron sputtering coating machine. After fabrication of devices, their geometries were confirmed by JEOL JSM-7800F scanning electron microscope.

Characterization: Powder X-ray diffraction (XRD) patterns were recorded on a Panaltical X'Pert-pro MPD X-ray power diffractometer using Cu Kα radiation (λ=1.54056 Å). Scanning electron microscope (SEM) was performed on a JEOL JSM-7800F scanning electron microscope. Transmission electron microscope (TEM) was performed on JEOL JEM-2100F electron microscope operated at 200 kV. X-ray

photoelectron spectroscopy (XPS) spectra were recorded using an ESCALAB 250 Xi XPS system of Thermo Scientific, where the base pressure in analysis chamber was 1.5×10^{-9} mbar and the X-ray spot was 500 μm. Photoluminescence spectra (PL) were detected using a FLS980 Pro Spectrofluorophotometer at room temperature with the excitation line at 330 nm from a 450 W Xe lamp. The time-resolved PL spectra were recorded by the same instrument coupled with a time-correlated single-photo-counting system at room temperature. UV-Vis diffuse reflection absorption spectra of the samples were obtained by a Varian Cary 5000 UV-Vis spectrometer equipped with an integrating sphere accessory and $BaSO_4$ as a reference material. Inductively coupled plasma optical

Optoelectronic characteristics: The electrical characterization was performed by means of a cryogenic probe station (CRX-6.5K, Lakeshore) connected to semiconductor characterization system (4200 SCS, Keithley) at room temperature. For photodetection, a broadband laser-driven light source (EQ-1500, Energetiq) calibrated by an UV-enhanced silicon photodiode provided an incident light, while the time responses were recorded by a current meter after the light illumination switch on-off.

Calculation of the R、EQE and D

We can obtain these parameters by using the following formulas:

$R= I_{ph}/PS$, $EQE= R_\lambda hc/e\lambda$, and $D=R_\lambda S^{1/2}/(2eI_d)^{1/2}$, where I_{ph} is the photocurrent of photodetectors, P is the intensity of illumination light, S is the effective areas, h is the Plank constant, c is the velocity of light, e is electron charge, I_d is the dark current of photodetectors.

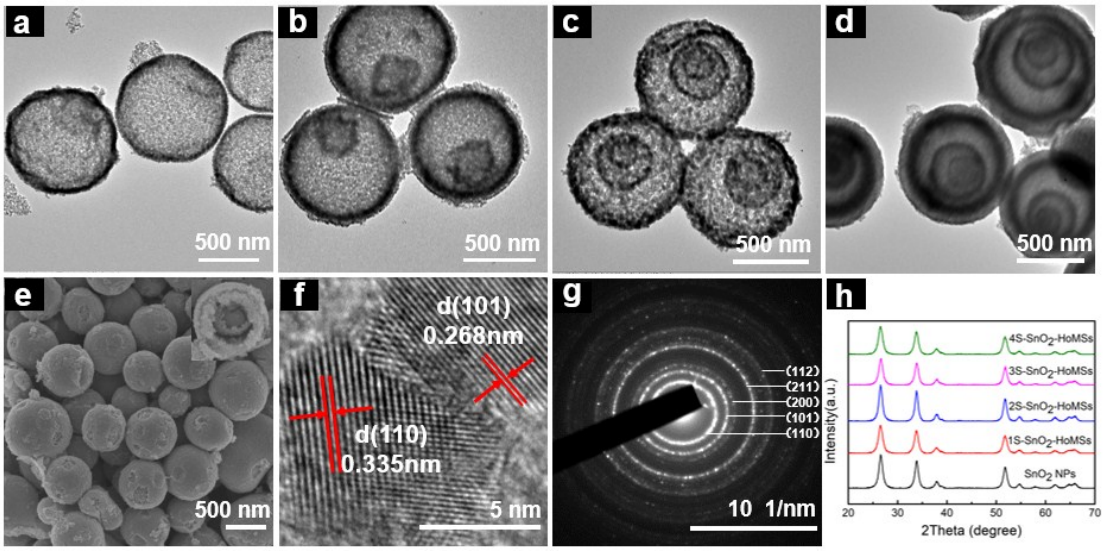

Figure S1. TEM images of a) single (1S-), b) double (2S-), and c) triple (3S-), d) quadruple (4S-) shelled SnO_2 HoMSs; e) SEM image of 4S-SnO_2 HoMSs; f) HRTEM image of the building-block on 4S-SnO_2 HoMSs; g) the selected-area electron di□raction (SAED) pattern of SnO_2 HoMSs ; h) XRD patterns of 1S-, 2S-, 3S-, 4S-SnO_2 HoMSs and SnO_2 nanoparticles.

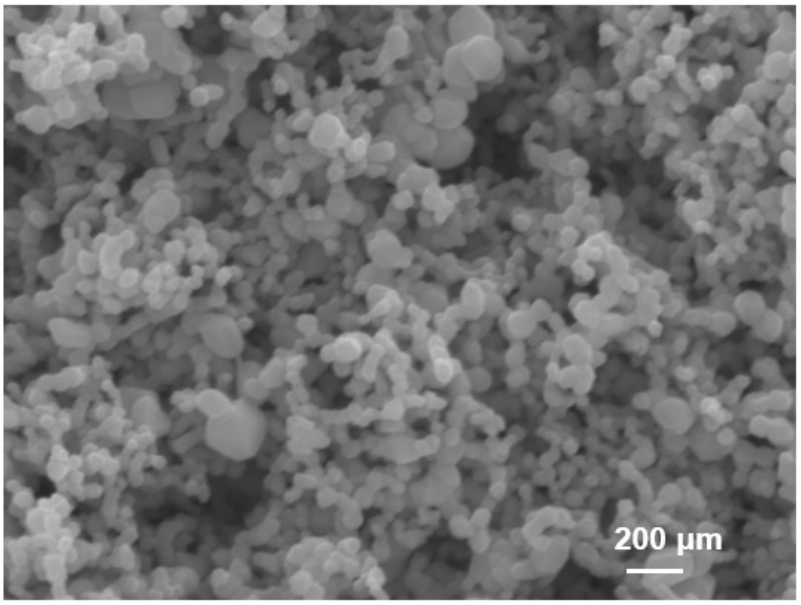

Figure S2. SEM image of SnO_2 nanoparticles.

SEM image (Figure S2) displays a nanoparticle structure with an average diameter size of about 45 nm. XRD patterns (Figure S1h) exhibit the same rutile phase of SnO_2 nanoparticles as SnO_2 HoMSs.

Table S1. The structure characteristics of SnO_2 HoMSs.

sample	grain size (nm)	diameter (nm)	shell thickness (nm)	intershell space (nm)
1s-HoMSs	15.61	903	48	-
2s-HoMSs	13.25	846	63 (1st)	189 (1st-2nd)
			73 (2nd)	-
3s-HoMSs	16.11	653	26 (1st)	48 (1st-2nd)
			26 (2nd)	113 (2nd-3rd)
			56 (3rd)	-
4s-HoMSs	14.82	989	38 (1st)	60 (1st-2nd)
			51 (2nd)	99 (2nd-3rd)
			83 (3rd)	46 (3rd-4th)
			31 (4th)	-

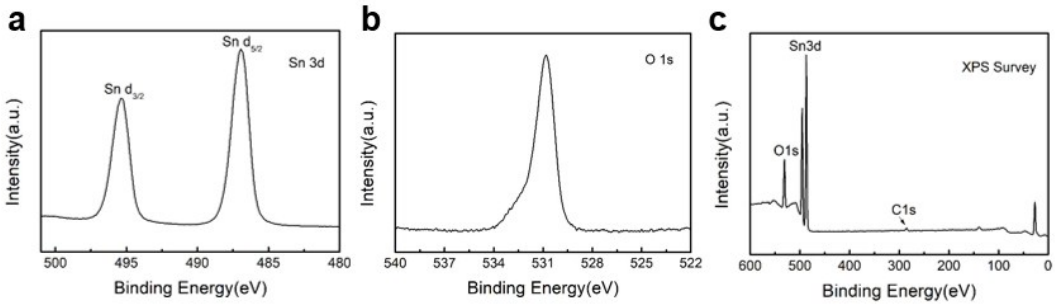

Figure S3. High-resolution XPS spectra of a) Sn 3d; b) O 1s; and c) XPS survey curves of 4S-SnO_2 HoMSs.

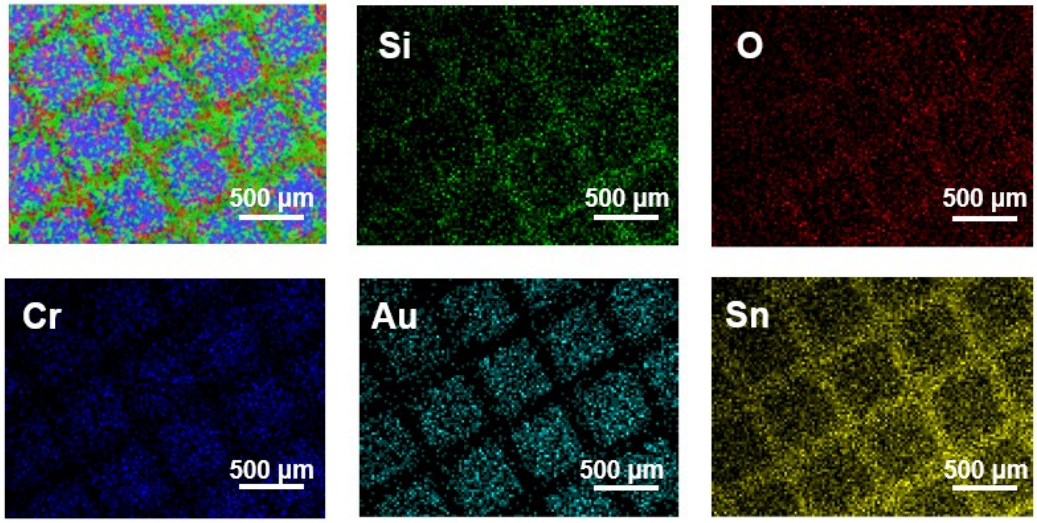

Figure S4. The elemental mappings of the SnO_2 HoMSs photodetectors.

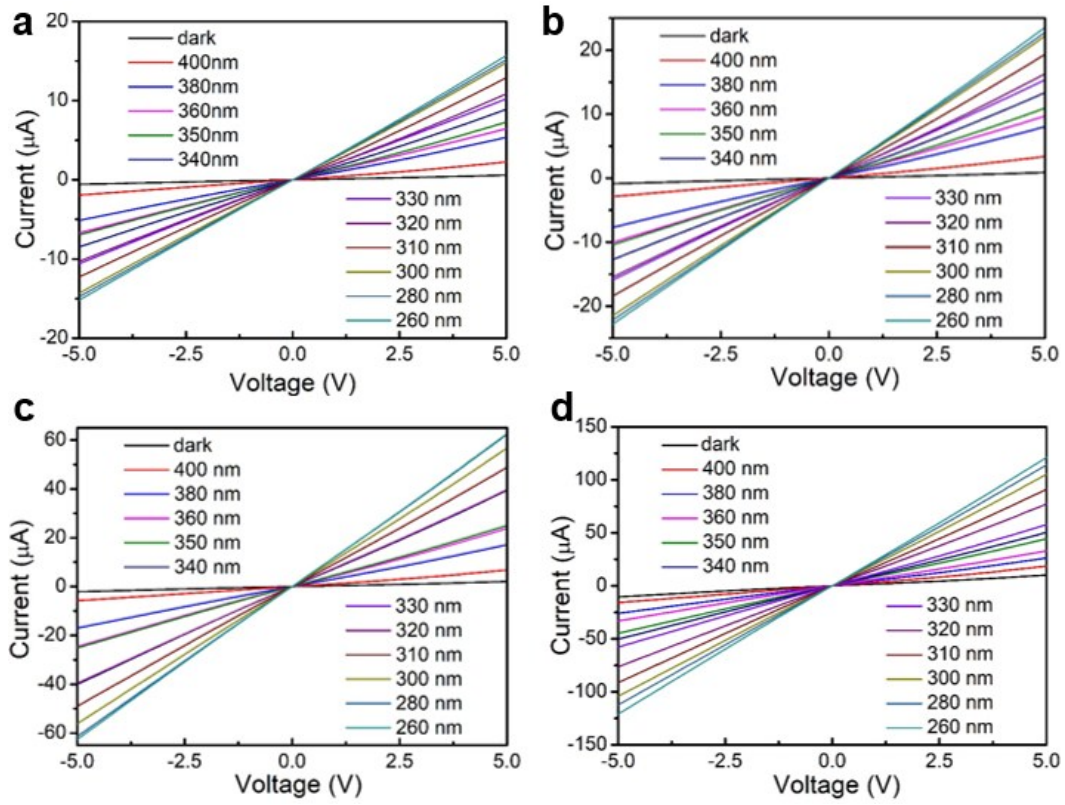

Figure S5. The I-V characteristics of (a) NPs, (b) 1S-, (c) 2S-, (d) 3S-SnO_2 HoMSs photodetectors illuminated with UV light from 260 nm to 400 nm and under dark condition.

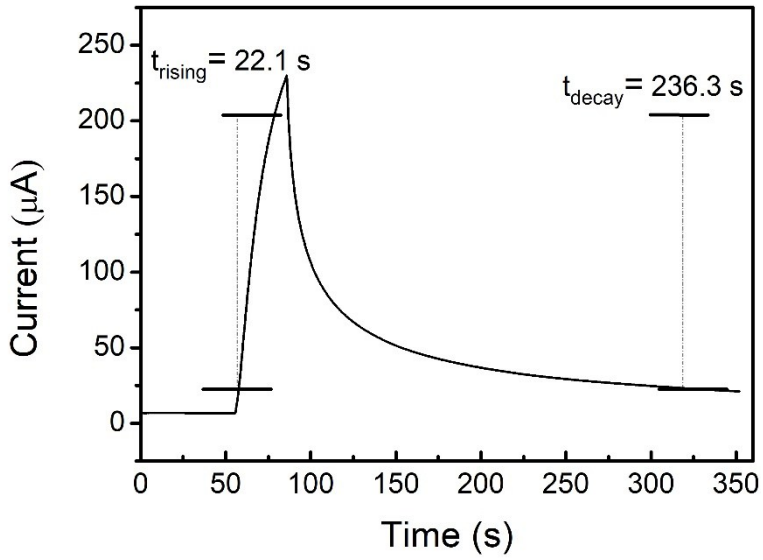

Figure S6. Time-resolved photo-response for 4S-SnO_2 HoMSs photodetectors.

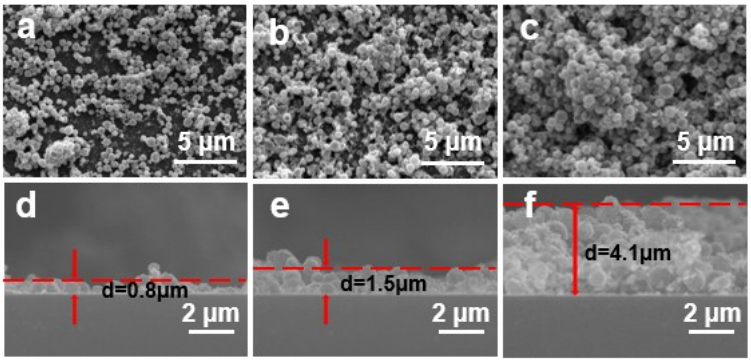

Figure S7. a), b) and c) SEM images of the surface states after screen printing by (a) once, (b) twice and (c) four times. d), e) and f) are cross-section SEM images of the corresponding films, respectively.

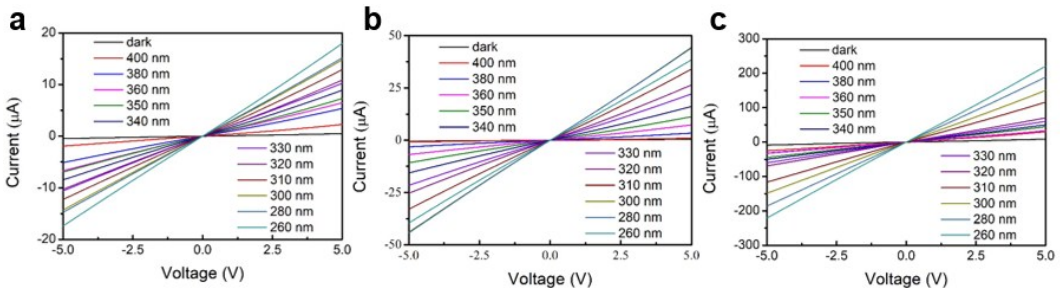

Figure S8. I-V curves of 4S-SnO_2-HoMS-film after screen printing for (a) once, (b) twice and (c) four times.

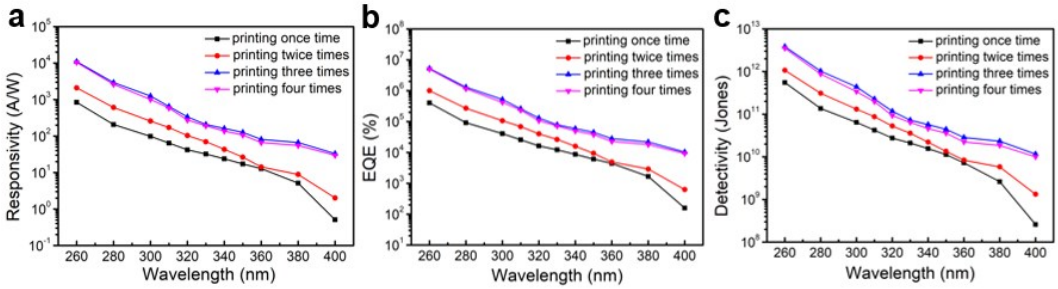

Figure S9. a) Responsivity, b) External quantum efficiency, and c) Detectivity of different 4S-SnO_2-HoMS-photodetectors after screen printing for different times.

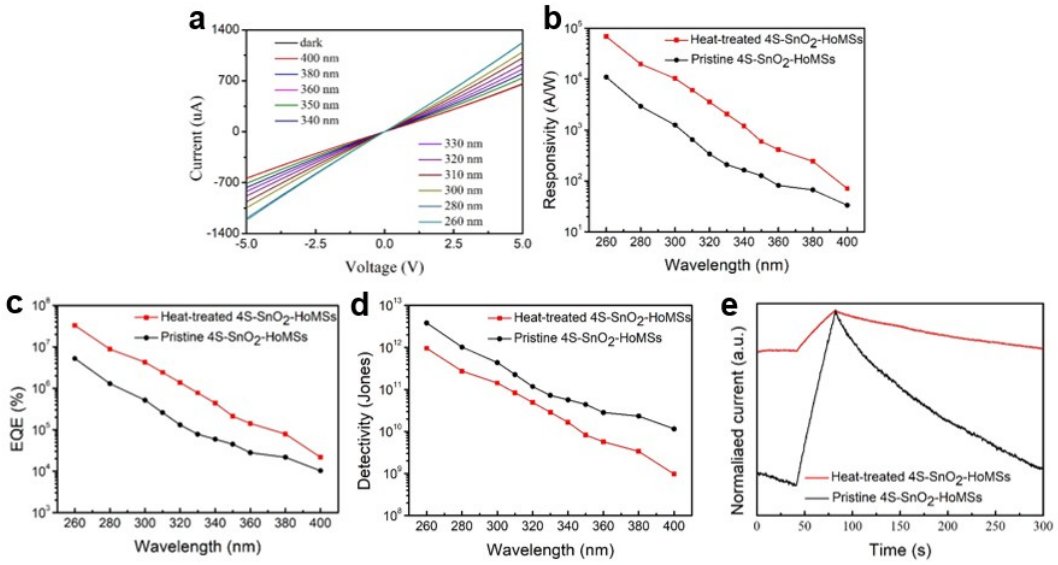

Figure S10. a) I-V characteristics of heat-treated 4S-SnO_2 HoMSs photodetectors at 150^{o}C under Ar atmosphere for 2 hours. b) Responsivity, c) External quantum efficiency, d) Detectivity and e) Time-dependent response of comparations about pristine and heat-treated 4S-SnO_2 HoMSs photodetectors.

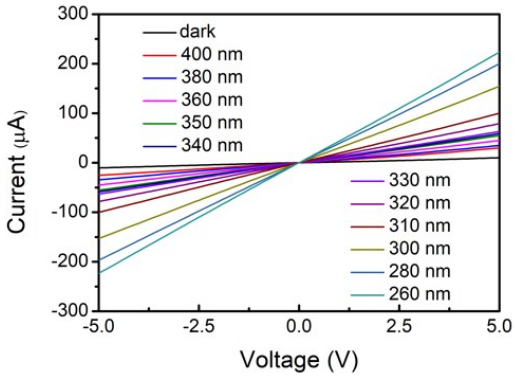

Figure S11. I-V curves of 4S-SnO_2 HoMSs photodetector after storing for about six month under the room condition in a Petri dishes.

The champion device of 4S-SnO_2 HoMSs in this work was fabricated about six month ago, and it was stored under the room condition in a Petri dishes. We retested such device by using the same method and the I-V results were displayed in Figure S11. Compared with the original I-V curves (Figure 3b), Figure S11 displayed the same tendency of photocurrent.

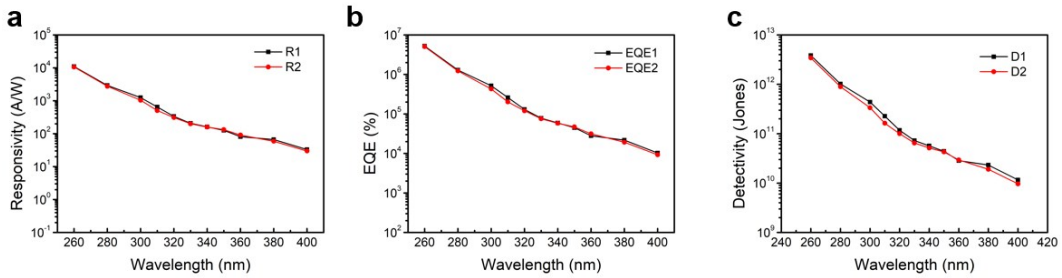

Figure S12. The comparation in photoelectric properties between pristine (R1, EQE1, and D1) and stored (R2, EQE2, and D2) 4S-SnO_2 HoMSs photodetector: (a) Responsivity; (b) EQE; (c) Detectivity.

Further, we calculated the R, EQE, and D of the stored 4S-SnO_2 HoMSs based device and marked them as R2, EQE2, and D2, respectively. Compared with R1, EQE1, and D1 of the pristine device, all of R2、EQE2、D2 displayed the same tendencies (Figure S12). Therefore, we can conclude that it illustrates a good stability of SnO_2-HoMSs photodetector.

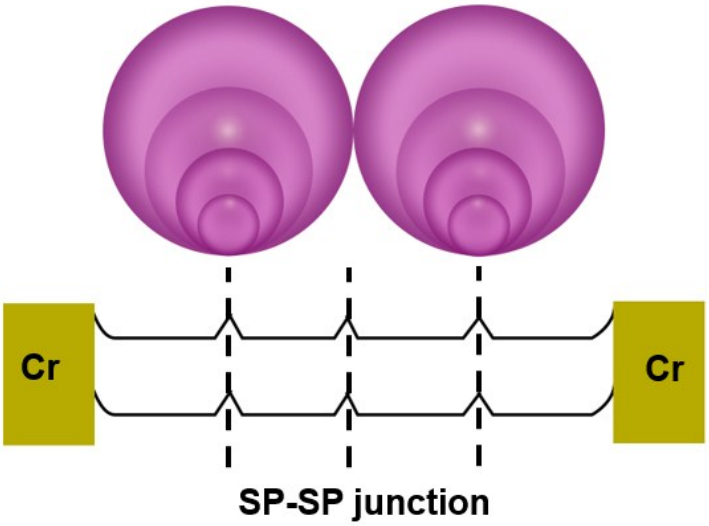

Figure S13. Schematic plot of the SP-SP junction barriers, and corresponding electron band diagram for the 4S-SnO_2 HoMSs.

Table S2. The comparison of photodetectors performance in other works.

Photodetectors	Photocurrent	Dark current	Responsivity	EQE(%)	Detectivity	references
SnO_2 microrod	-/1V	13μA/1V	3×10^8 AW^{-1}	1.5×10^9	1.50×10^9 Jones	1
SnO_2/CuZnS microwire	-/1V	4.0 nA/3V	27.6 AW^{-1}	-	5.41×10^{11} Jones	2
Monolayer SnO_2 nanonet	232.3μA/1V	65.5μA/1V	-	-	-	3
SnO_2 nanowire	2.1μA/1V	19.4 nA/1V	-	1.32×10^9	-	4
SnO_2 nanowire	15.7μA/5V	-/5V	4.3×10^4 AW^{-1}	1.94×10^5	2.32×10^{13} Jones	5
ZnO hollow sphere	1.9μA/3V	2pA/3V	35.9 AW^{-1}	-	-	6
4S-SnO_2 HoMSs (Pristine)	231.0 μA/5V	9.7 μA/5V	1.01×10^4 AW^{-1}	5.23×10^6	3.83×10^{12} Jones	This work
4S-SnO_2 HoMSs (Heat-treated)	1230.2μA/5V	653.4 μA/5V	6.88×10^4 AW^{-1}	3.28×10^7	9.53×10^{11} Jones	This work
Perovskite	-/5V	-/5V	over 4.0×10^3 AW^{-1}	over 10^4	over 10^{13} Jones	7
ZnO hollow sphere	2.62μA/5V	0.05μA/5V	13.5 AW^{-1}	-	-	8
SnO_2@ZnO	-/5V	-/5V	100 AW^{-1}	-	-	9
Ga_2O_3:Zn	5.3μA/3V	16nA/5V	1.05 AW^{-1}	5.12×10^2	4.9×10^{11}Jones	10
Perovskite nanowire arrays	-/5V	-/5V	1.25×10^4 AW^{-1}	-	1.73×10^{11}Jones	11
$MoSe_2$ hollow sphere	-/5V	-/5V	8.9 AW^{-1}	3.05×10^3	7.9×10^9Jones	12

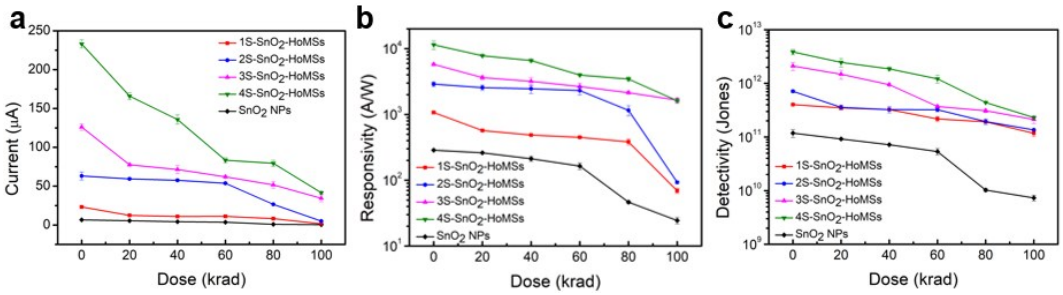

Figure S14. SnO_2 HoMSs photodetector performance under γ irradiation**.** a) I-V characteristics; b) Responsivity and c) Detectivity of 1S-, 2S-, 3S-, 4S-SnO_2 HoMSs and SnO_2 NPs photodetectors measured with different irradiation dose from 0 to 100 krad at 260 nm with 5 V.

References

[1] Liu K, Sakurai M, Aono M, et al. Ultrahigh-Gain Single SnO_2 Microrod Photoconductor on Flexible Substrate with Fast Recovery Speed[J]. Advanced Functional Materials, 2015, 25(21): 3157-3163.

[2] Cai J, Xu X, Su L, et al. Self-Powered n-SnO_2/p-CuZnS Core–Shell Microwire UV Photodetector with Optimized Performance[J]. Advanced Optical Materials, 2018, 6(15): 1800213.

[3] Hao C, Hu L, Fang X, et al. General Fabrication of Monolayer SnO_2 Nanonets for High-Performance Ultraviolet Photodetectors[J]. Advanced Functional Materials, 2012, 22(6):1229-1235.

[4] Hu L, Yan J, Liao M, et al. Ultrahigh external quantum efficiency from thin SnO_2 nanowire ultraviolet photodetectors[J]. small, 2011, 7(8): 1012-1017.

[5] Yan J, Chen Y, Wang X, et al. High-performance solar-blind SnO_2 nanowire photodetectors assembled using optical tweezers[J]. Nanoscale, 2019, 11(5): 2162-2169.

[6] Wang X, Liao M, Zhong Y, et al. ZnO Hollow Spheres with Double-Yolk Egg Structure for High-Performance Photocatalysts and Photodetectors[J]. Advanced Materials, 2012, 24(25): 3421-3425.

[7] Saidaminov M I, Adinolfi V, Comin R, et al. Planar-integrated single-crystalline perovskite photodetectors[J]. Nature communications, 2015, 6: 8724.

[8] Chen M, Hu L, Xu J, et al. ZnO hollow-sphere nanofilm-based high-performance and low-cost photodetector[J]. Small, 2011, 7(17): 2449-2453.

[9] Hu M, Teng F, Chen H, et al. Novel Ω-Shaped Core–Shell Photodetector with High Ultraviolet Selectivity and Enhanced Responsivity[J]. Advanced Functional Materials, 2017, 27(47): 1704477.

[10] Li Y, Zhang D, Lin R, et al. Graphene Interdigital Electrodes for Improving Sensitivity in a Ga_2O_3: Zn Deep-Ultraviolet Photoconductive Detector[J]. ACS applied materials & interfaces, 2018, 11(1): 1013-1020.

[11] Deng W, Huang L, Xu X, et al. Ultrahigh-responsivity photodetectors from perovskite nanowire arrays for sequentially tunable spectral measurement[J]. Nano letters, 2017, 17(4): 2482-2489.

[12] Chen X, Yang H, Liu G, et al. Hollow Spherical Nanoshell Arrays of 2D Layered Semiconductor for High-Performance Photodetector Device[J]. Advanced Functional Materials, 2018, 28(8): 1705153.